Variations in the photo-saturation current on Solar Orbiter

Felix Helena Holma

13.12.2021

Supervisor: Niklas J. T. Edberg

Examiner: Andreas Korn

Contents

1 Abstract

We investigate how the photo-saturation current of the Radio and Plasma Waves instrument aboard the Solar Orbiter spacecraft responds to variations in solar illumination as well as to solar flares and energetic particle impacts, and model its remaining variations in order to predict its behaviour over the forthcoming years. Predicting the behaviour of this current is important for operating the instrument in an optimal fashion.

We normalize the time series of the photo-saturation current with respect to variations in solar illumination and find that, while the largest effect comes from distance to the Sun, it also exhibits a dependence on solar activity. Furthermore, both the overall amplitude for a specific level of activity and the slope of the proportionality decrease with time as the instrument reacts progressively less strongly to variations in illumination. We propose that this is due to degradation of the material of the probe. Modeling the material degradation as a combination of two exponentially decreasing outgassing processes, desorption and decomposition with time dependencies of around three weeks and three years respectively, predicts that the photo-saturation current will reach values about a fifth of its current amplitude by the beginning of the extended mission phase in five years time.

We conclude that while some decrease of the photo-saturation current may be mitigated by heightened solar illumination when solar maximum is reached towards the end of the nominal mission phase, by the next solar minimum, the photo-saturation current will have decreased to such an extent that electric field measurements with the Radio and Plasma Waves instrument become difficult. We find no correlation of variations in the photo-saturation current with solar flares, but due to a small sample size, we cannot rule a causal relationship out either. We also show that any effect from energetic particle impacts, if observed so far, must be far weaker than those for which we can establish variations of other parameters as the source.

2 Introduction

In this project we investigate how the photo-saturation current, as measured by the Radio and Plasma Waves analyser (RPW) on the Solar Orbiter mission, varies with solar illumination and other possible contributing factors, such as solar flares and energetic particle impacts. We then try to model the photo-saturation current, as predictions of its behaviour are needed for operating the RPW instrument and ensure good measurements in the future.

Solar Orbiter (SolO) aims to explore the Sun and inner heliosphere, and was launched on February 10th 2020 with a nominal mission duration of seven years followed by an extended mission duration of three years. SolO is an ESA-led ESA/NASA collaboration and part of ESA's Cosmic Vision 2015-2025 programme, and carries ten instruments, six of which are for remote-sensing and four for in-situ measurements. The goal of the mission is to investigate the question "How does the Sun create and control the heliosphere – and why does solar activity change with time?". This overarching objective can be specified into four key questions concerning (1) the origin of the coronal magnetic field and what drives the solar wind, (2) how the heliosphere varies with solar transients, (3) how energetic particles are produced in solar eruptions, and (4) how the solar dynamo works and drives the connection between the Sun and the heliosphere [1].

SolO will get as close to the Sun as 0.28 AU, reaching a minimum perihelion that lies within the orbit of Mercury. Observation of the polar regions will be made possible during the extended mission phase when SolO reaches a heliographic latitude of 34°. The combination of remote-sensing and in-situ measurements is meant to provide a full description of the solar wind plasma, and the conditions under which it originates on the Sun and is transported outwards into the solar system [1, 2].

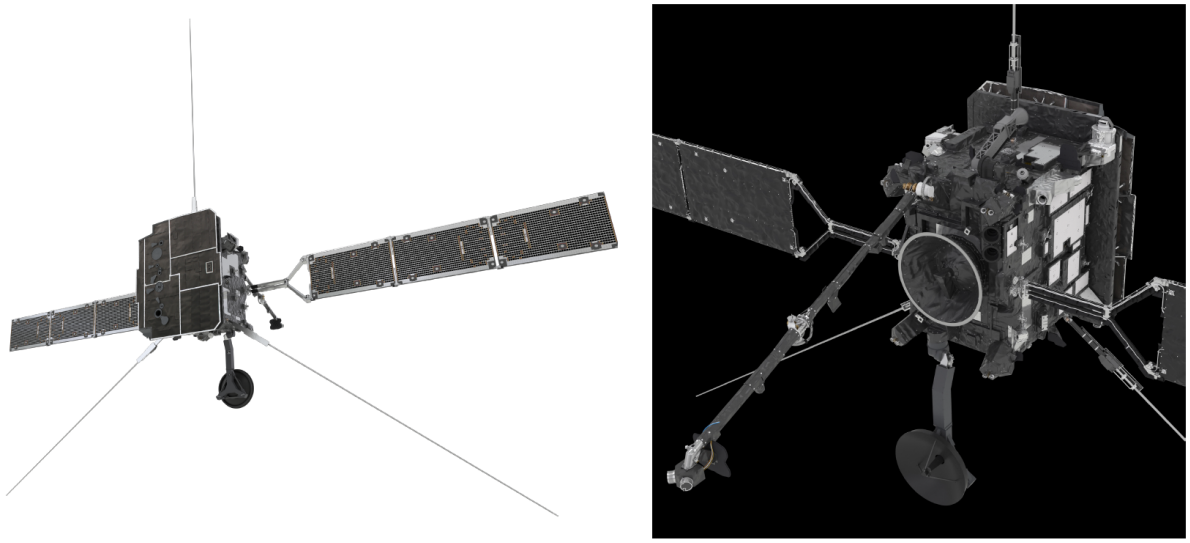

Figure 1: Sun-facing front-view of Solar Orbiter (left), and rear-view (right) [1].

RPW will play a role in answering almost all of the SolO mission's key questions. For example, in recent first results, the probe-to-spacecraft potential measured by RPW was used to derive the plasma density in the solar wind, and specifically its fluctuations on small timescales. The power spectra and time-series for these density fluctuations, combined with fluctuations of the magnetic field measured by another instrument, were used to characterize the observed waves and turbulence. These results, along with future measurements, will significantly contribute to our understanding of the solar wind [3].

RPW comprises several different detectors, and one of its tasks is to measure electric fields. In order to ensure high quality measurements, the antenna potential must be kept close to the surrounding plasma potential. This can be achieved by keeping the bias current fed to the probe just below the photo-saturation current [4]. Predicting how the photo-saturation current will vary in response to the Sun's behaviour is thus important for operational purposes.

In section 3, we will give a background of RPW and the photo-saturation current, followed by the parameters whose influence we will investigate, namely solar intensity and activity, solar flares, energetic particle fluxes, and finally material properties. In section 4, we describe the data analysis process and present the results, and in section 5 we discuss their implications and relevance for operations. Finally, in section 6 we give a summary of this work.

3 Background

3.1 The RPW instrument and the photo-saturation current

RPW is one of the four in-situ instruments aboard SolO and measures electric and magnetic fields as well as solar radio emissions. The data can be used to characterize the plasma and different types of waves in the solar wind. RPW consists of several detectors and will be needed in answering almost all of SolO's main scientific objectives.

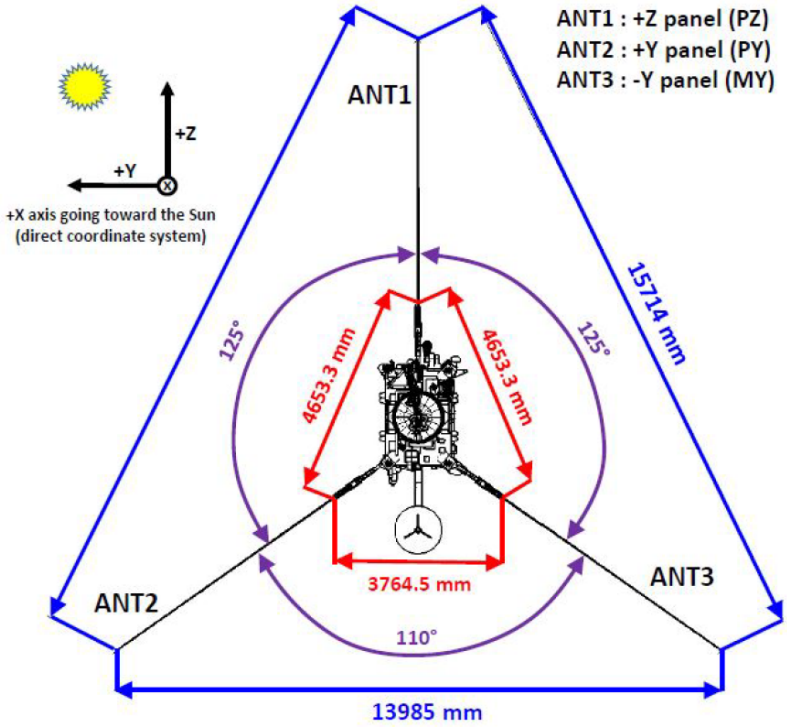

Figure 2: Configuration of RPW's three antennas in their rest position on SolO. During flight, their tips may move up to 1.5 m due to changes in temperature. The antennas are in a plane perpendicular to the direction from SolO to the Sun [4].

In this project we have analyzed data from the electric antenna subsystem (ANT), which comprises three antennas spanning a plane facing the Sun. The antennas consist of 6.5 m monopoles making up the electrical sensor, fastened in 1 m booms, which can be individually deployed from the spacecraft. The antenna potential can also be varied independently through the bias current fed to the antennas [4]. Antennas 2 and 3 were later coated with a protective additional layer of paint as it turned out more light than first expected would be reflected onto them. In the solar wind, the antennas are continuously subject to ions, electrons, and radiation from the Sun. Electrons are light and easily repelled by a negative potential, while ions, due to their larger mass, will not be affected as much. Sunlight hitting the antennas can cause electrons to be emitted through the photoelectric effect, and these then give rise to the photo-saturation current, I_{ph0}, when they are repelled by the negative potential.

For an electric field measurement, the antenna biasing unit (BIAS) sets the current bias I to each of the antennas to a value between -60 and +60 μA, shifting the antenna

potential U. Which bias current should be set depends on the local plasma potential. Ideally, the antenna potential should be close to the plasma potential. This is achieved by keeping the bias current fed to the probe just below I_{ph0}, and, as will be detailed below, allows for higher accuracy and lower noise in the measurements of the potential between the antennas, from which the electric field can then be derived. In order to determine I_{ph0}, regular sweeps are performed on the three antennas, where I is varied between 2.5 and -15 μA and the resulting U is measured [4]. Such a sweep is shown in fig. 3 as a dependence of I on U.

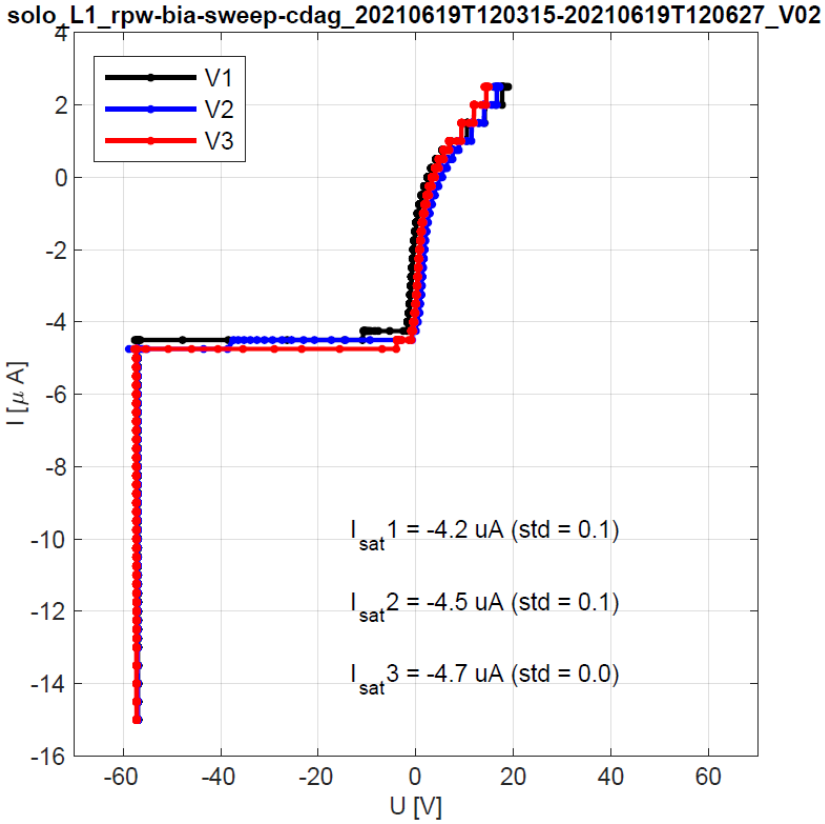

Figure 3: Example of a sweep performed on the RPW ANT subsystem, where I is varied and the resulting U is measured. Antennas 1, 2, and 3 are shown in black, blue, and red. For $U<0$ we see I_{ph0} at -4.2, -4.5, and -4.7 μA for the three antennas. The region where (in absolute values) I is just below I_{ph0} and dI/dU is the steepest is where measurements of the electric field with the instrument will show the highest accuracy.

We see that for $U<0$ we get a constant I around -4.5 μA regardless of potential. While all incoming electrons from the solar wind are repelled, there is a small contribution from ions already directed towards the antenna. However, this current is negligible as there are so few particles and the projected area of the antenna is so small. What makes up most of the resulting current is instead I_{ph0} from the photoelectric effect. For I just below I_{ph0} (in absolute values), meaning for $U>0$, we see a region of very steep dI/dU. If we operate the instrument in this range, a small change in U (due to a change in the electric field) will give rise to a large difference in I, and thus the measurement will be more accurate. Thus, we want an accurate value of I_{ph0} so that we can set our bias current just below it.

As this current has to be set some week in advance, predicting the behaviour of I_{ph0} is important for operating the RPW instrument. For that purpose, we will investigate the influence of several parameters on I_{ph0}.

As radiation from the Sun is what induces I_{ph0} in the antennas in the first place, the influence of solar illumination on I_{ph0} will be investigated both in the form of overall solar activity as well as solar flares, which occur on shorter timescales. It can also be assumed that kinetic energy can be transferred to the antennas by impacts of energetic particles, causing electrons to be emitted and thereby creating an additional current which would be measured in addition to I_{ph0}. Whether this effect is noticeable in the data will therefore also be investigated.

3.2 The $F_{10.7}$ index as a proxy for solar activity

The 10.7 cm solar radio flux, also called the $F_{10.7}$ index, measures the average total emission in a 100 MHz band centered around 2800 MHz, corresponding to a wavelength of 10.7 cm, from the entire solar disk over a time of some 20 minutes spaced out over an hour. The units are solar flux units (sfu), where 1 sfu = $10^{-22}\mathrm{Wm}^{-2}\mathrm{Hz}^{-1}$. Three such measurements are made at set times in the evening each day, from which daily and hourly averages can be extrapolated [5].

The $F_{10.7}$ index can be correlated to and used as a proxy for other, less easily measurable quantities, and is, next to sunspot number, the most widely used indicator of overall solar activity. Solar activity comprises several different emission mechanisms on the Sun, which may be located at different positions on the disk and vary with time independently from each other. For example, emissions from solar flares usually vary on millisecond scales, but active regions tend to form and decay over days or months, and the 11-year solar cycle shows variations on even longer timescales. Apart from the quiet Sun background and bursts of activity on much shorter timescales, one component is particularly sensitive to conditions in the upper chromosphere and the base of the corona. This is where a lot of thermal free-free emission occurs, especially in active regions where plasma is held in place by magnetic fields. This particular component is therefore a good measure of overall solar activity, and is, as it shows a spectral peak at wavelengths around 10 cm, the reason the $F_{10.7}$ index is useful as an indicator of the level of solar activity [5].

As the $F_{10.7}$ index includes emissions from mechanisms which may vary rather fast, extrapolating an activity level from the time of measurement to any other time during the day is problematic. Furthermore, as these emission mechanisms may vary in how their radioemission correlates with emissions in other wavelengths, and the components cannot usually be easily distinguished, there is no reliable way to use the $F_{10.7}$ index to estimate the flux density at another wavelength with truly dependable accuracy [5]. This could pose an issue in this report, as we are interested in UV rather than radio emissions, as the Sun radiates more in the shorter wavelengths. Using the $F_{10.7}$ index as a proxy for overall solar activity therefore introduces some uncertainty into our results. However, this issue is more severe in periods of high solar activity when short timescale events are more frequent, while most of our data is from 2020, which was at solar minimum, and 2021, which, while we can expect higher uncertainty than for the year before, is still closer to solar minimum than maximum.

3.3 Solar flares

Solar flares are sudden and highly localized increases in brightness on the Sun, usually occuring close to sunspots in active regions. They are believed to be generated when magnetic reconnection accelerates plasma in the solar corona downwards along the magnetic fieldlines until the particles are stopped by the higher plasma density, heating them up. This causes chromospheric plasma to well up into the so called coronal loops, which are loops of magnetic fieldlines protruding up into the corona from the photosphere and below. In the coronal loops, the plasma cools over a couple of minutes by radiating first in the X-ray and then in the extreme ultaviolet (EUV) wavelengths [6].

As this cooling is a free-free emission process, flares radiate isotropically, and can thus be observed by any observer within the same hemisphere [7]. However, as the plasma densities in the coronal loops during a solar flare are up to four orders of magnitudes higher than usual in the corona, some limb darkening may occur due to the emitted radiation having to pass through more material which is not as optically thin. The irradiance for flares located 45° from the disk center can be 10% lower than it would be right in the center. However, limb darkening is not uniform as a function of wavelength, so irradiance in the EUV may be affected differently than in the X-ray [6].

An observed solar flare is usually catalogued with its start, peak and end time, the location of the respective active region (AR location) on the Sun, and its X-ray class. The AR location is given as a longitude and latitude in a heliographic coordinate system, meaning that the location of a feature on the solar surface is described by the position it visibly appears at on the solar disk as seen from Earth. As the Sun exhibits differential rotation, with rotational period of an individual feature being dependent on both latitude and also how it anchors magnetically to the photosphere, the coordinates of an active region, sunspot or solar flare will only hold true for a specific time, which must be given alongside the location to completely describe the catalogued event [8].

The X-ray class describes the peak brightness in the X-ray wavelength range. The Geostationary Operational Environmental Satellite (GOES) uses 1 minute averages in the 1-8 Å band [9]. X-ray classes are given as a logarithmic scale of letters (A, B, C, M and X in order of increasing brightness) followed by a number for smaller steps, making an M1 flare ten times as bright as a C1 flare, where C corresponds to a value of at least 10^{-6} Wm^{-2}. However, it must be kept in mind that a flare's X-ray class only describes a small part of the spectrum of emitted radiation, and that other wavelengths which do not necessarily correlate with the X-ray class may also play a role. Furthermore, flares are more frequent at solar maximum [7], so since we are looking at data from solar minimum we will not have such a large sample and any connection with our data may be harder to spot.

3.4 The EPD instrument and energetic particle fluxes

Energetic particles are mainly released during eruptive events on the Sun such as solar flares and coronal mass ejections. The Energetic Particle Detector (EPD) is one of SolO's in-situ instruments and measures electrons, protons and ions across a wide energy range, and will be central to answer question 3 of the scientific objectives as well as contribute with supporting measurements to the other questions.

EPD includes four sensors for different, partially overlapping energy ranges [10]. In

this project, we analyze data from the SupraThermal Electron Proton (STEP) sensor, which detects particles in the lowest end of the measured energy range. As most of the flux comes from lower-energy particles, which are already enough to emit electrons from the RPW antennas, we assume this lower-energy particle flux to be sufficient to investigate any correlation with I_{ph0}. Nonetheless, taking data from the other sensors into account as well would show a more complete picture.

STEP consists of two sensor heads, one of which is called the "magnet channel" and contains a magnet that prevents electrons from reaching the sensor head. The other is called "integral channel" and measures all particles with energies of 2-80 keV. Thus, by subtracting the magnet channel count rate from that of the integral channel, the electron count rate can be obtained [10].

3.5 Spacecraft outgassing and material degradation processes

When a spacecraft and the instruments it carries are subject to the environment of space, particles leave the material through different mechanisms in a process called outgassing, which can never be completely prevented. This can create a gas cloud around the spacecraft which may interfere with certain measurements. Here, however, we are interested in how outgassing may change the material properties of the antennas of SolO's RPW instrument, and thus affect the measurements taken with it.

Depending on the mechanism, the process will need a different activation energy E_a, which is characteristic for the material in question and can be provided by, for example, radiation from the Sun. Furthermore, temperature T will impact the extent to which a process occurs. The amount of outgassing by a specific process follows the form $e^{-\frac{E_a}{RT}}$ where R is the gas constant. This can also be expressed as the outgassing being proportional to $e^{-\frac{t}{t_d}}$ where t is the time and t_d the time dependence or 1/e decay time, meaning the time when the outgassing has decreased to its original value over e. Mechanisms with lower activation energies thus make the material decay faster, and increased temperatures speed up the process [11].

The main outgassing mechanisms are desorption, diffusion and decomposition. Outgassing occurs from the entire bulk of the material, but since we only look for mechanisms affecting the photo-saturation current, which depends on photo-emission on the surface of the antenna, we do not have to take diffusion into account here. However, desorption of water and other outgassing products that have previously been adsorbed onto the surface while SolO was still on Earth is to be expected. This mechanism is also strongly temperature dependent, and has been recorded on spacecraft even after years in space. However, the initial activation energy is low, so it decreases very quickly in the beginning. Additionally, decomposition of the material will occur as it naturally degrades when it ages, albeit on a longer timescale, with a lower temperature dependence and a higher activation energy [11].

4 Data analysis

In this section, we characterize the variation of I_{ph0} with various parameters. We begin in subsections 4.1 and 4.2 with the most obvious parameter, the solar intensity, which depends on both the distance R to the Sun and the solar activity, for which we use the 10.7 cm solar radio flux, the $F_{10.7}$ index, as a proxy. We then look at possible variations with solar flares in subsection 4.3, and variation with energetic particle fluxes in subsection 4.4. Finally, after normalizing for all those variations, we try to characterize the remaining I_{ph0} variation in subsection 4.5, using a model that attributes the variation to changes in material properties.

4.1 Variation with distance R to the Sun

As per the inverse square law, intensity of radiation from the Sun at some position (x,y,z) is inversely proportional to the square of the distance $R = \sqrt{x^2 + y^2 + z^2}$ to the Sun.

We can already see from the first two panels of fig. 4 that SolO's distance to the Sun has a huge effect on I_{ph0}, as the largest variation matches perfectly with the variation of R, most notably at perihelion in the middle of june 2020 as well as february and september 2021. We normalize I_{ph0} with respect to variation of R by multiplying with R^2, which is shown in the third panel. This smooths the data significantly, especially for the later datapoints.

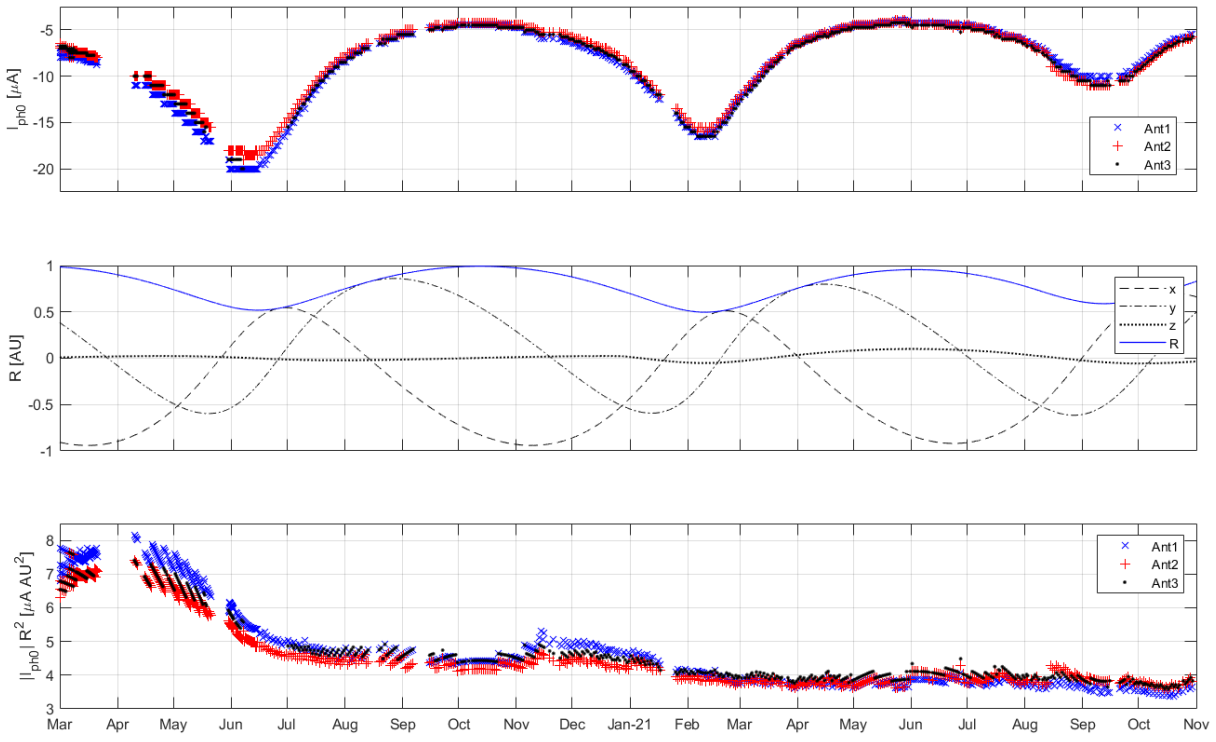

Figure 4: Time series of I_{ph0} (a), the distance R from SolO to the Sun (b), and the normalization of I_{ph0} with respect to distance R from the Sun (c).

4.2 Variation with solar activity

Intensity of solar illumination is furthermore affected by solar activity. In order to normalize for this effect as well, we use the $F_{10.7}$ index as a proxy for variations in intensity across all wavelengths. The $F_{10.7}$ data [12] is an extrapolation from three measurements a day on Earth and is shown in the first panel of fig. 5. Again, we have to use the inverse square law to scale this intensity to how it would be at the distance of SolO. This is shown in the second panel, and illustrates that although there certainly is some variation in solar intensity with solar activity, at SolO's distance (around 0.4 to 1.0 AU during the pictured time interval), it is not as high as variation with R. For example, while the solar intensity almost doubled with spikes in activity during November and December 2020, this is only noticeable as minor peaks when SolO's orbit is taken into account. The third panel shows I_{ph0} normalized with respect to both distance to the Sun and solar activity levels.

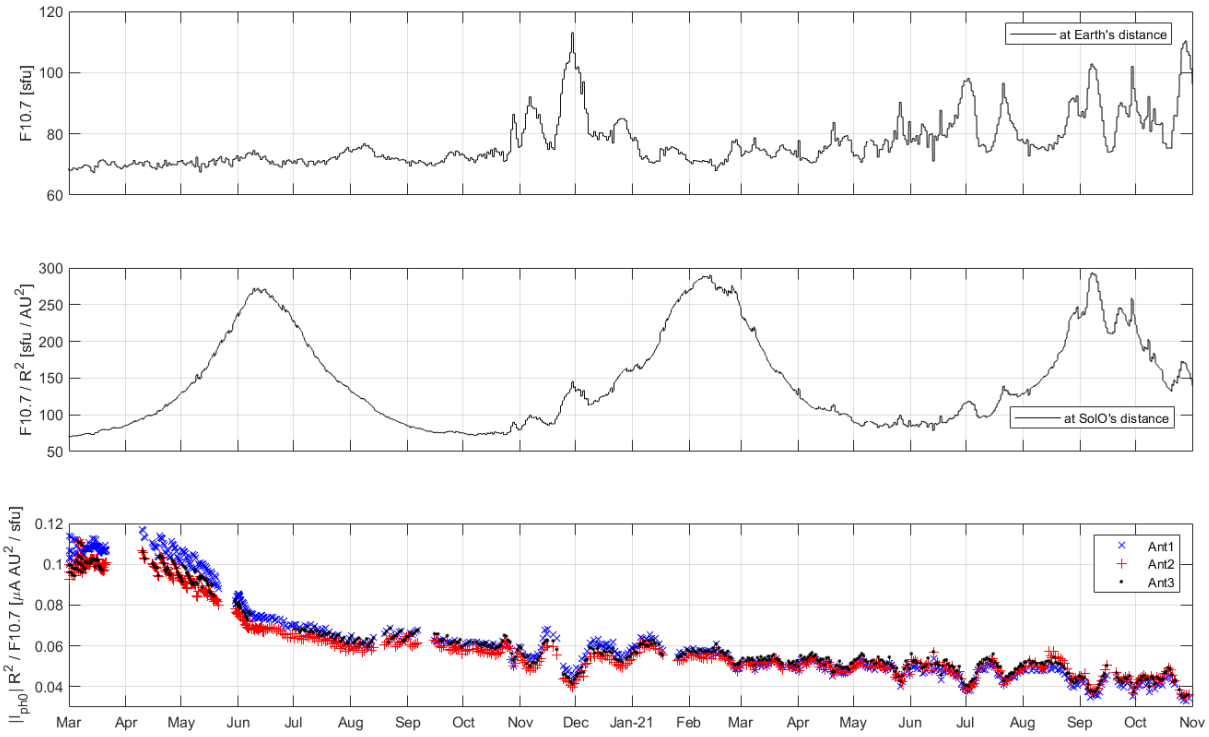

Figure 5: $F_{10.7}$ as measured on Earth (a), scaling of $F_{10.7}$ to SolO's position (b), and normalization of I_{ph0} with both R and $F_{10.7}$ (c).

However, it needs to be taken into consideration that the Sun does not radiate equally from its entire surface area, but rather may have active regions, which may either be directed towards or away from an observer at Earth or SolO. Furthermore, SolO and Earth may be up to 180° apart in their orbits around the Sun, and thus not necessarily subject to the same solar activity. However, as solar rotation at the equator has a period of approximately 24.47 days, barring any changes in activity while the Sun rotates, they will eventually experience the same activity, albeit shifted in time.

In fact, this solar rotation period is already evident in the $F_{10.7}$ data in fig. 5, where in the top panel the three major peaks of activity around November and December 2020 are approximately one solar rotation apart. We interpret this as prolonged heightened

activity in some region of the Sun that faces Earth during these three periods. The activity itself is assumed to first rise and then diminish in intensity, as the middle peak (from the second time the active region faces Earth) is clearly the highest, and the lower ones are almost of equal height.

We now try three different ways to compensate for the difference in perspective SolO and Earth have of the Sun, and extrapolate how $F_{10.7}$ would have varied at SolO based on the measurements from Earth.

The first method utilizes a simple linear timeshift, either forwards or backwards, with the goal of smoothing the I_{ph0} data by normalizing for any influence of $F_{10.7}$ variations. The most notable features of the $F_{10.7}$ data are the peaks around November and December 2020, while most other features either drown in the much larger variation with R, or, for the later part of 2021, are similar in magnitude but not as distinct. Therefore, for this method, we make use of the positions of SolO and Earth during November and December 2020 to calculate how many days forwards or backwards the $F_{10.7}$ data needs to be shifted before normalizing I_{ph0} with respect to it.

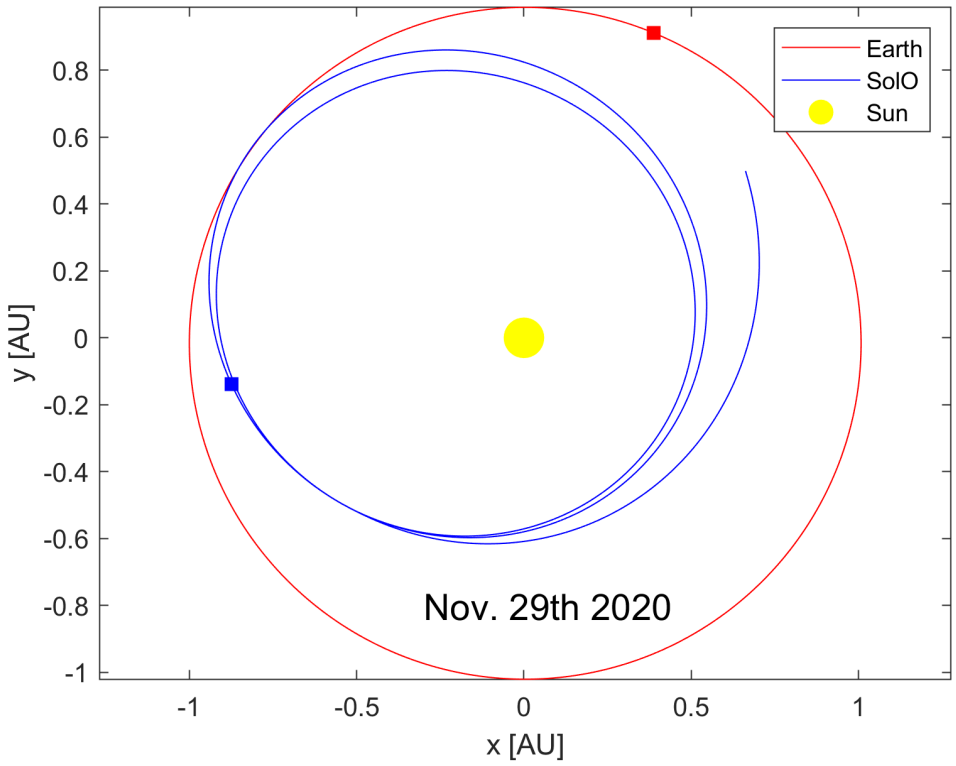

Figure 6: Orbits of Earth and SolO around the Sun during the time period for which I_{ph0} data has been presented, along with their positions on November 29th 2020, shown in the ECLIPJ2000 coordinate system, where the x-axis points to the vernal equinox, the z-axis to the north ecliptic pole and the y-axis completes the right-handed system. Solar rotation at the equator as well as movement along the orbits of SolO and Earth all occur counterclockwise.

The first panel in fig. 7 shows that, for the most part, the angle between SolO and Earth does not change very rapidly. Specifically, during the most notable period of solar activity in November and December 2020, it remains largely constant. Fig. 6 shows that

Earth and SolO in the middle of this period are roughly 120° apart. Both SolO's and Earth's movement as well as the solar rotation at the equator occur in the counterclockwise direction from this perspective. This implies that an active region of the Sun observed on Earth would face SolO about a third of the Sun's rotational period later, or have already faced it two thirds of the Sun's rotational period earlier. Thus, we have the option of shifting the $F_{10.7}$ data from Earth either about 16 days back in time, or 8 days forward, in order to get the activity likely observed by SolO. This is shown in the second panel of fig. 7, and the normalizations of I_{ph0} by these $F_{10.7}$ are shown in panels three and four of fig. 8.

For the second method, instead of approximating a suitable forwards- and backwards timeshift based on only the most notable peaks in the data, we now calculate the possible forwards and backwards timeshift for every individual datapoint based on the positions of SolO and Earth at that time, and then choose the shorter one, as that solar activity statistically runs a lower risk of changing during the time needed for rotation.

From the positions (x,y,z) of SolO and Earth we can easily calculate their respective longitude (we disregard the z-component as SolO's height over the ecliptic at this point in the mission does not noticeably impact which parts of the Sun are visible from it compared to from Earth), defined as an angle $0° < \theta_{\mathrm{i}} < 360°$ in counterclockwise direction from the 0° position.

Thus, the angle $\alpha_1 = \theta_{\mathrm{SolO}} - \theta_{\mathrm{Earth}}$ will be $-360° < \alpha_1 < 360°$. The absolute value of this angle is now proportional to the number of days the datapoint needs to be shifted, and the sign signifies direction of the shift. However, for values $|\alpha_1| > 180°$ we instead use the conjugate of the absolute value of the angle and change the sign, as the shortest timeshift will now be in the opposite direction. This angle is then:

$$\alpha_2 = -(360° - |\alpha_1|) \tag{1}$$

We now convert the angle into a number of days t for the datapoint to be shifted:

$$t = 24.47 \frac{\alpha_i}{360°} \tag{2}$$

where 24.47 is the rotation period of the Sun at the equator in days, and α_i and thus t may be positive or negative. We then add t to the timestamp of the datapoint, to compensate for the rotation time of the Sun between the angles facing SolO and Earth. The resulting timeshifted $F_{10.7}$ is shown in the bottom panel of fig. 7, and the thus normalized I_{ph0} datapoints are shown in panel five of fig. 8.

Finally, for the third method, we instead calculate both the forwards and backwards timeshift, and take their average weighted by the length of the respective other timeshift so that, ultimately, a longer timeshift gets a lower weight. We first calculate $\alpha_1 = \theta_{\mathrm{SolO}} - \theta_{\mathrm{Earth}}$ the same way as before, resulting in a value $-360° < \alpha_1 < 360°$, which may lead to either a forwards shift (for absolute values $< 180°$) or a backwards shift (for absolute values $> 180°$). In order to get the shift in the respective other direction, we find the conjugate of the absolute value of the angle, and change the sign:

$$\alpha_2 = -\frac{\alpha_1}{|\alpha_1|}(360° - |\alpha_1|) \tag{3}$$

We calculate the timeshift this corresponds to the same way as before, giving us t_1 and t_2. Note that these aren't strictly forwards or backwards, but rather can be either or, but will always be complementary for each individual datapoint. We then calculate the datapoints as shifted by both t_1 and t_2 separately. The corresponding weights w_i, where i is 1 or 2, are calculated as

$$w_i = 1 - \left| \frac{t_i}{24.47} \right| \tag{4}$$

where, once again, 24.47 is the rotational period of the Sun at the equator in days, and the weights should add up to 1 as a sanity check. Finally, we calculate each $F_{10.7}$ datapoint as an average of those shifted by t_1 and t_2 multiplied by their respective weights. The resulting timeshifted $F_{10.7}$ is shown in panel three of fig. 7, and the I_{ph0} data normalized with this shifted $F_{10.7}$ is shown in the final panel of fig. 8.

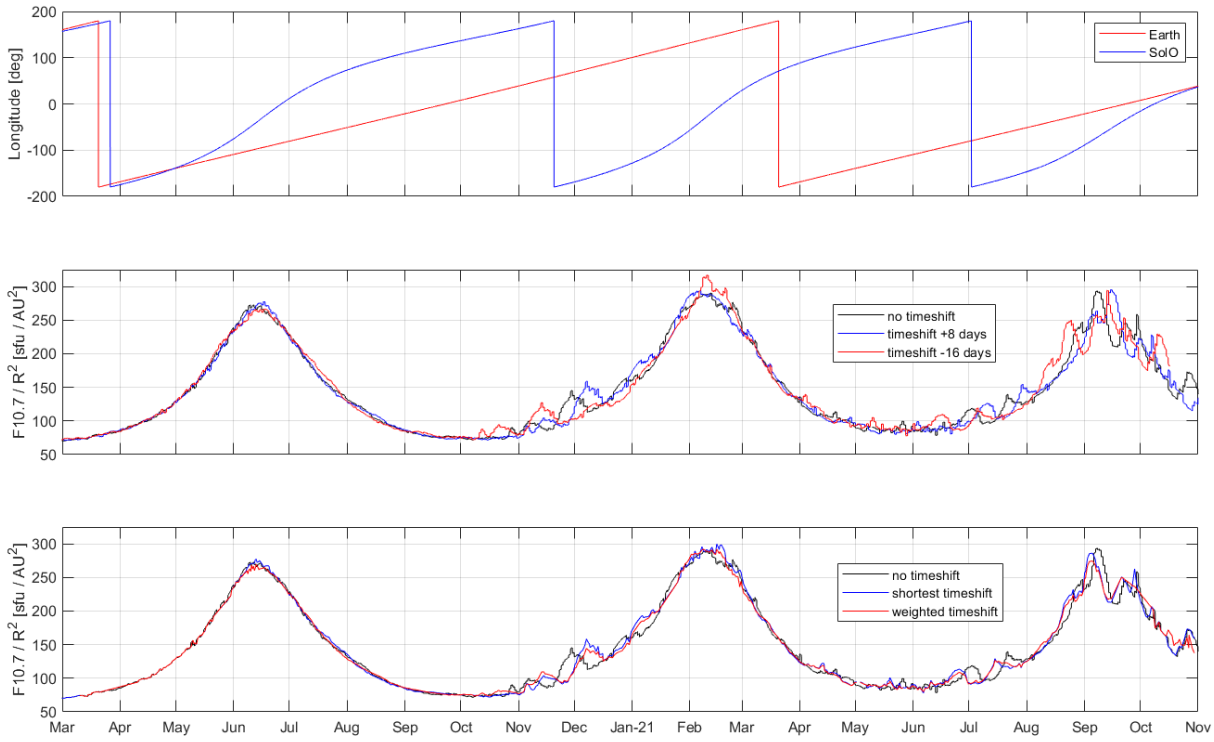

Figure 7: Time series of longitudes of SolO and Earth (a), and unshifted values of $F_{10.7}$ at the distance of SolO compared to values timeshifted by two set amounts of days (b) and values timeshifted by the shortest respective timeshift and the weighted timeshift (c).

We now see what these timeshifts would lead to in terms of normalizing I_{ph0} with them. The best fit would be the one that smoothes the data out the most, as the normalization is meant to remove the influence of any changes in solar activity.

We see, as can be expected, that the weighted timeshift provides the smoothest curve and can thus be assumed to be the best normalization. Therefore, this is the normalization that we use henceforth.

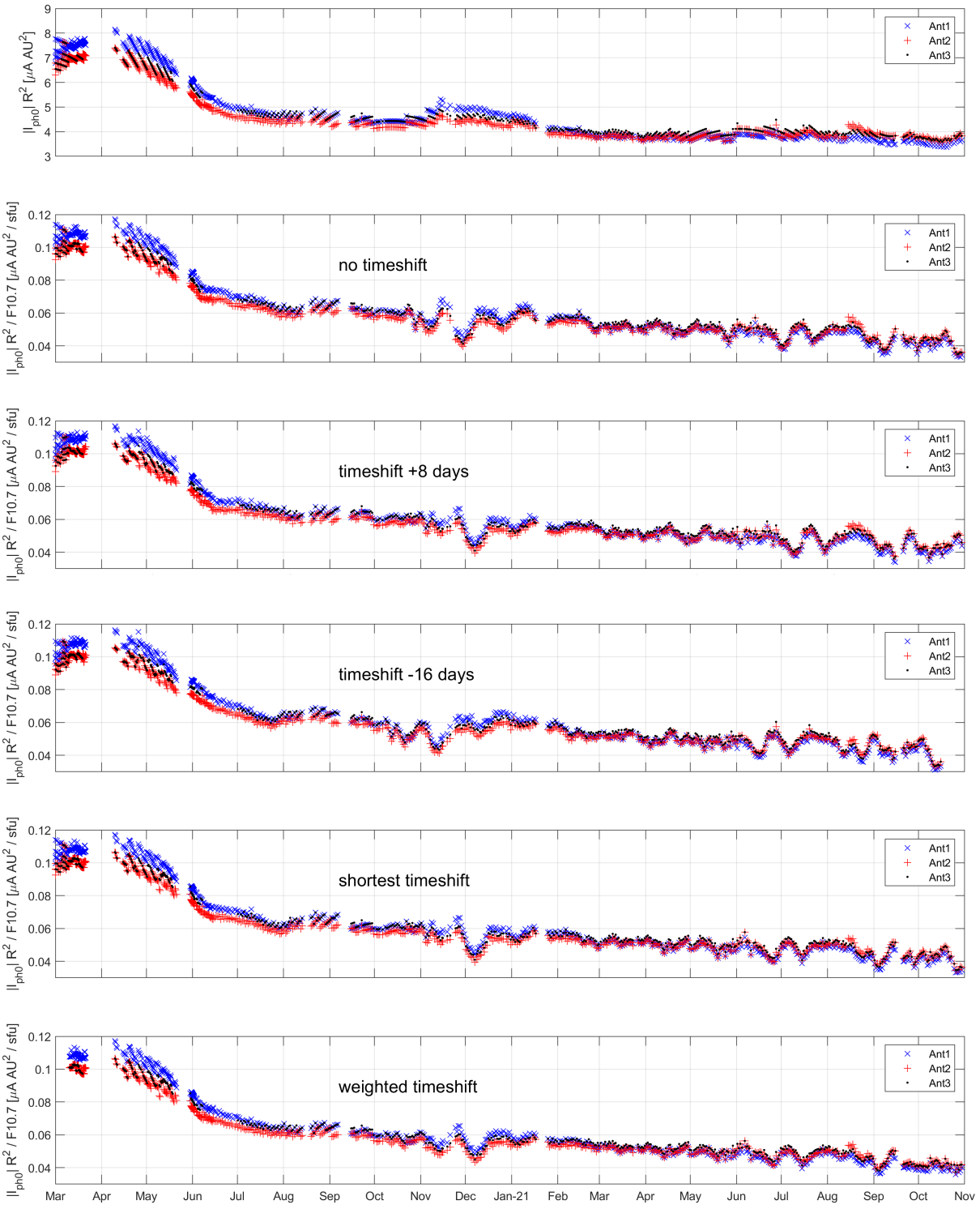

Figure 8: Time series of I_{ph0} normalized with respect to R (a), with respect to R and the $F_{10.7}$ value at the distance of SolO (though not necessarily its position in its orbit) (b), and with respect to R and $F_{10.7}$ at SolO's distance to the Sun timeshifted by the three different methods described above: eight days forward (c), 16 days backward (d), the shortest timeshift for each individual datapoint (e), and a weighted timeshift of the forwards- and backwards-shifted value (f). The weighted timeshift produces the smoothest result.

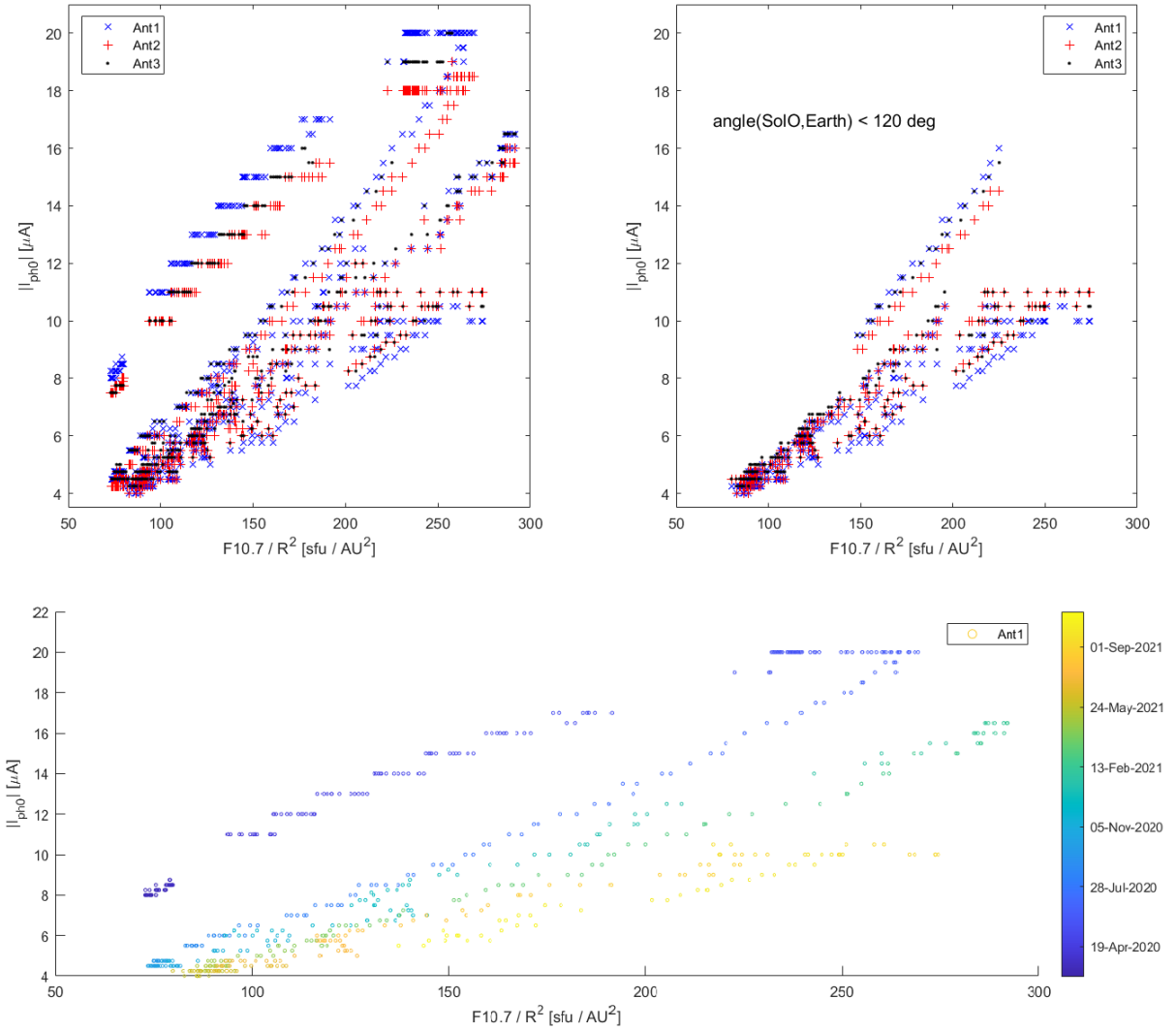

Figure 9: Dependence of I_{ph0} on $\mathrm{F}_{10.7}$ as normalized to SolO's distance (top panels), where all datapoints are included on the left hand side and only datapoints for which the angle between SolO and Earth was $< 120°$ are shown on the right hand side. Dependence of I_{ph0} on $\mathrm{F}_{10.7}$ as normalized to SolO's distance for antenna 1 with a colour bar to showcase the datapoint's chronological order (bottom panel).

We can gauge the extent of the influence of solar activity on I_{ph0} from fig. 9. We see in the upper panels how I_{ph0} varies with $\mathrm{F}_{10.7}$ as normalized to SolO's distance. The panel on the left includes all datapoints whereas the panel on the right limits datapoints to only those for which SolO and Earth where $<120°$ apart, so as to reduce the influence of any error introduced by the timeshift of the $\mathrm{F}_{10.7}$ index. Furthermore, all datapoints before July 1st 2020 have been removed due to showing comparably large variations for which the source has not been established. In fig. 9, we see that I_{ph0} varies fairly linearly with the solar activity as experienced at SolO's position. This is especially prominent when only considering the limited set of datapoints on the right hand side, which can be assumed to be more accurate. This linear trend appears to occur in several separate segments, only partially visible in the limited data set, which showcase slightly different slopes and amplitudes. As the bottom panel illustrates, the segments are actually periods of time

occurring after one another, with the highest amplitude and highest slope belonging to the earlier measurements, and the most recent ones having both lower overall amplitude and a lower slope.

This indicates that the amplitude of I_{ph0} depends on solar activity in a linear fashion, but that the exact proportionality is subject to some change with time. Specifically, the change is two-fold: firstly, the overall amplitude of I_{ph0} for a specific level of solar activity decreases with time, and secondly, the slope of the proportionality also decreases with time, meaning that the instrument reacts progressively less strongly to an increase in solar activity. Why this may be the case is further explored in section 4.5.

4.3 Influence of solar flares

Having normalized I_{ph0} for the effects of solar intensity, we now investigate if other features in the data can be explained by any known solar flares. We use the Hinode Flare Catalogue [13] and a list of the top 50 solar flares of the year [9] to find flares with an X-ray class of C or higher that occurred in 2020 and 2021 respectively. Since the end of 2021 saw comparably more solar flares, we chose a minimum X-ray class of C5.5 for the second half of that year. As these flares were observed from Earth, they naturally do not include possible flares from the side of the Sun not facing Earth at the time, although SolO may have observed them. Conversely, we must reject any flares that were visible from Earth but could not have been observed from SolO.

As mentioned in section 3.3, radiation from solar flares spreads almost hemispherically through the upper layers of the Sun, only being dimmed somewhat at large angles. Therefore, as a selection criterion, we require only that the flare occurred in the solar hemisphere visible to SolO at the time of occurence. If several flares occurred in the same active region on the same day, only the strongest one was noted. Table 1 lists the flares that were visible from SolO according to this selection process.

The flares are indicated with red lines in fig. 10. We see that none of them can be clearly identified in the normalized I_{ph0} data in panel three. Although some flares coincide with peaks in the data, for a comparably sudden event like a flare we rather expect an abrupt jump than a broad peak. Also, far from all of the flares coincide with peaks in the I_{ph0} data, and we do not see higher peaks for higher X-ray class solar flares (although this may be due to the I_{ph0} measurement coinciding with a weaker flare rather than the strongest one for that particular day, if there were several flares). In particular, for the three M-class flares in April and May 2021 we also know that this cannot be due to a variation in distance downscaling the intensity of stronger flares, as they all occur at approximately equal R, when SolO is close to aphelion. Towards the end of 2021, several flares occurred while SolO was close to perihelion. Despite also being among the flares with higher X-ray class, these flares do not generally coincide with higher I_{ph0} peaks. Although it can be argued that X-ray class need not necessarily scale with intensity across the entire wavelength spectrum that may influence I_{ph0}, no causal relation between the observed solar flares and variations in I_{ph0} can be established from this data alone.

Looking at the second panel in fig. 10, where I_{ph0} is normalized only with respect to R, we see no peaks coinciding with a solar flare, showing that any effect is, if present and detected, far weaker than that of overall solar activity.

Date	AR location	X-ray class
15.08.2020	N26W70	C2.0
16.10.2020	S26W86	C3.5
01.11.2020	S21W88	C3.4
28.11.2020	S25W89	C1.0
05.12.2020	S20W76	C1.2
09.03.2021	N19E68	C1.6
19.04.2021	S25E21	M1.1
07.05.2021	N18E70	M3.9
08.05.2021	N18E57	C8.7
09.05.2021	N18E45	C4.0
21.05.2021	N20E27	C6.2
22.05.2021	N22E11	M1.4
27.08.2021	S29E02	C7.4
28.08.2021	S27W11	M4.8
08.09.2021	S18E07	C8.4
23.09.2021	S28E10	M2.8
07.10.2021	N17E29	C5.5
09.10.2021	N17W01	M1.6
26.10.2021		M1.0
27.10.2021	S27E05	C8.6
28.10.2021	S26W09	X1.0
29.10.2021	N18E42	M1.5

Table 1: Highest X-ray class solar flares visible from SolO in 2020 [13] and 2021 [9]. No location was given for the flare on October 26th 2021 in the source; however, it would have been visible to SolO regardless of location as SolO was almost exactly on a line with Earth and the Sun at that time.

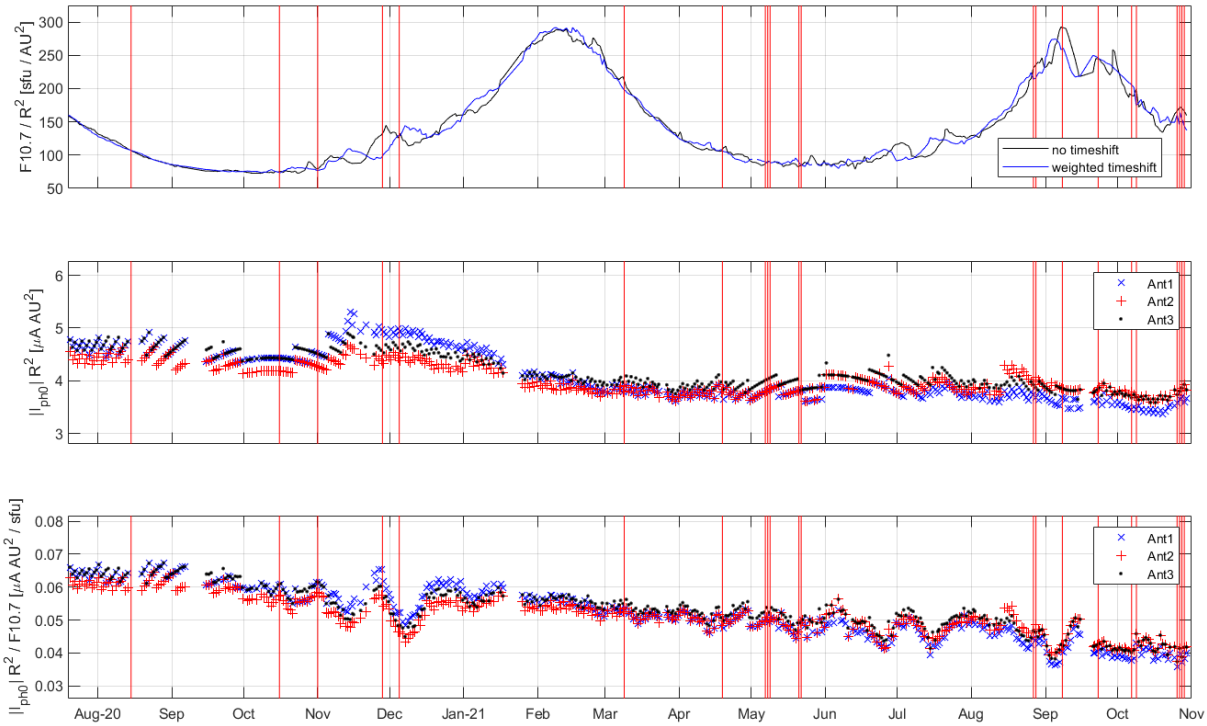

Figure 10: Solar flares visible from SolO indicated by red lines overlain on a time series of the $F_{10.7}$ index at SolO's position (a), I_{ph0} normalized by R (b), and I_{ph0} normalized by R and the timeshifted $F_{10.7}$ index (c).

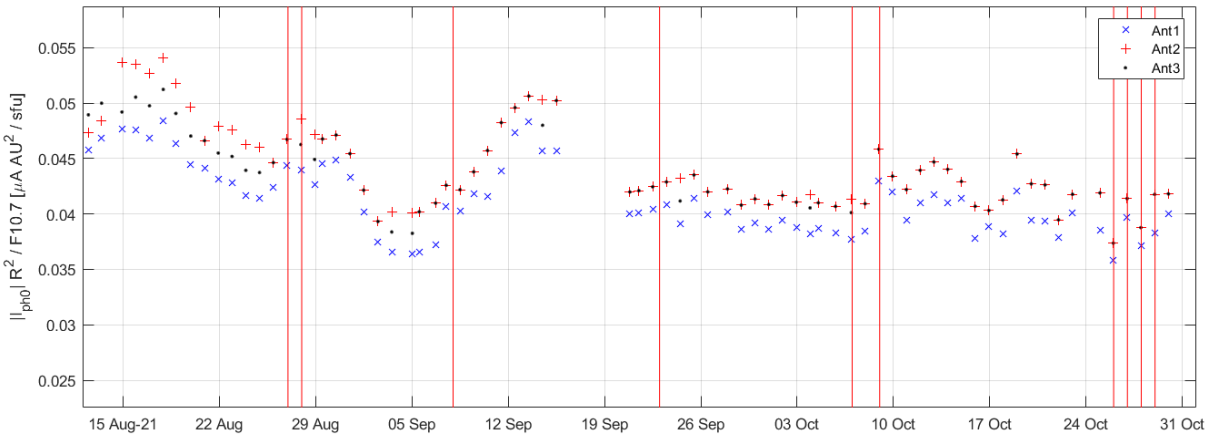

Figure 11: Time series of I_{ph0} for autumn 2021, with solar flares indicated by red vertical lines. Two flares, on August 28th and October 9th, coincide with a sudden increase in I_{ph0} for at least one of the antennas.

It must be kept in mind though that there is only one I_{ph0} datapoint a day, whereas solar flares occur on a timescale of minutes to an hour, at any time of the day. As our sample size of 22 flares is quite small, and flares were included regardless of the time of day they occurred, it is still possible that any variation of I_{ph0} caused by a solar flare would have been missed. Fig. 11 shows a time series of the solar flares and I_{ph0} during autumn 2021. Two flares, on August 28th and October 9th, coincide with a sudden jump

in I_{ph0} in at least one of the antennas, rather than just a broad peak. They were also both, as M-class flares, among the higher class flares of this sample, and both occurred approximately during the same time of day, shortly after 6 a.m, while I_{ph0} on those days was measured at noon. While the flares themselves, as characterized by a sudden and brief increase in X-ray output, thus cannot have been the direct cause of these sudden jumps in I_{ph0}, this could still be an indication that the respective active region displayed an increased output of ultraviolet radiation after the solar flare, which could then in turn be noticeable in I_{ph0}. However, more similar observations would be needed to fully establish this as a causal relationship.

4.4 Influence of energetic particle impacts

Having normalized I_{ph0} for solar intensity and having ruled out known solar flares as sources of any remaining features in the data, we investigate the possibility of energetic particle fluxes having a measurable influence on I_{ph0}.

We see in fig. 12 that energetic particle fluxes vary on rather short temporal scales. This means that any correlation between them and the I_{ph0} data may be difficult to identify, as some amount of uncertainty was introduced by the normalization of I_{ph0} with the timeshifted $\mathrm{F}_{10.7}$ index.

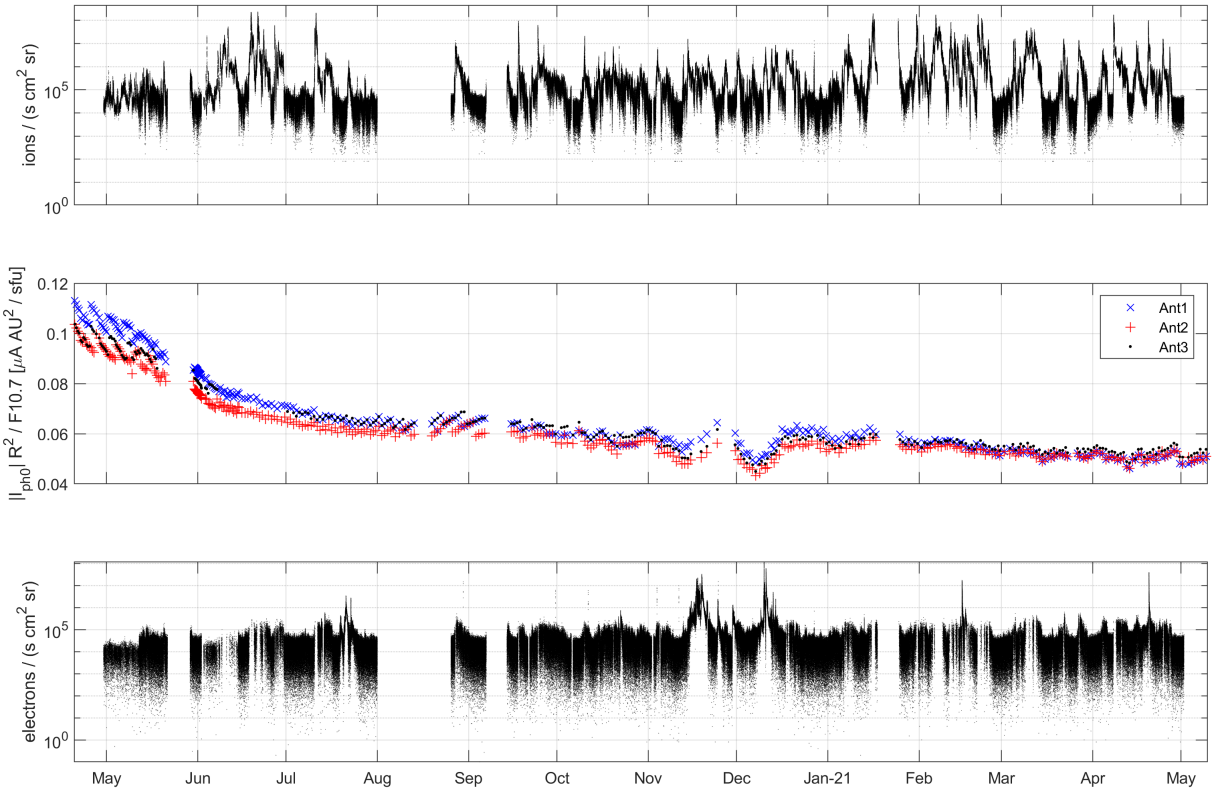

Figure 12: Time series of the energetic particle flux of ions (1), I_{ph0} normalized with respect to solar intensity (2), and the energetic particle flux of electrons (3).

The most notable feature in the electron flux is the two peaks in November and December 2020, coinciding with the known solar activity around that time and lining up

almost perfectly with the two most notable dips in the I_{ph0} data. This is unexpected, as particles, regardless of their charge, are thought to transfer kinetic energy to the antennas, causing secondary electron emission and thus an additional current rather than a decrease.

Looking instead at the ion flux, we see that there is a lot of variation on a timescale of weeks; however, it is irregular and does not seem to correlate with I_{ph0} in any discernable fashion. We can see a slight overall increase of the ion flux around perihelion around June 2020 and February 2021, but even the average of that effect is far weaker than the variation on a weekly or even daily timescale.

As the energy transferred by the energetic particles is kinetic and their charge does not impact the result, we look at ions and electrons combined in fig. 13. However, all but a few of the highest peaks of the particle flux still stem from ions, and the highest peaks of the particle flux do not in any systematic way coincide with the most notable features of I_{ph0}. We conclude that particle fluxes do not significantly impact I_{ph0} at a level that would be distinguishable from stronger influences caused by other parameters.

This is further illustrated in fig. 14, where I_{ph0} is plotted directly against the energetic particle flux. It is clear that variations between individual antennas exceed any dependence I_{ph0} may have on energetic particle fluxes. For all three antennas, any particle flux can coincide with practically any I_{ph0} value. The reason why, in particular, high particle fluxes contrary to expectations do not tend to coincide with high I_{ph0} values is due to the fact that they simply do not occur as often as lower fluxes, thus biasing our data. Furthermore, the segmentation of the datapoints into separate groups, as already observed in section 4.2, can be seen again. This proves that, as the highest I_{ph0} values are from the earliest measurements and even high particle fluxes do not bring I_{ph0} up to those previous levels again, energetic particle fluxes at the level hitherto experienced by SolO do not impact I_{ph0} to any measurable degree.

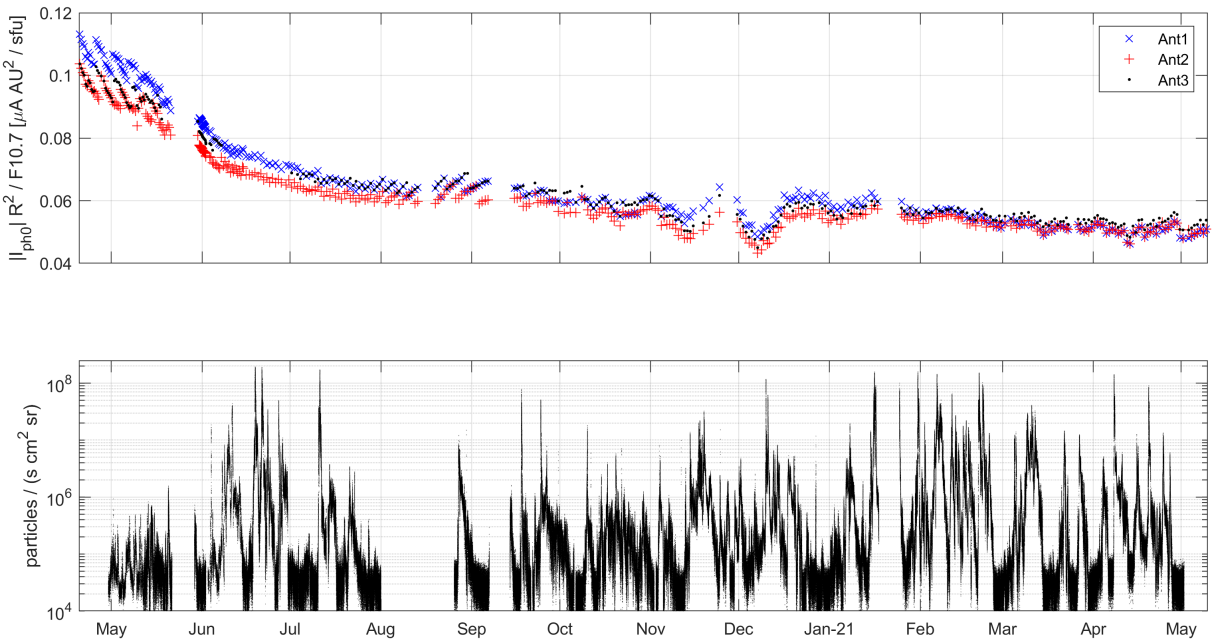

Figure 13: Time series of the normalized I_{ph0} (1) and particle fluxes of ions and electrons combined (2).

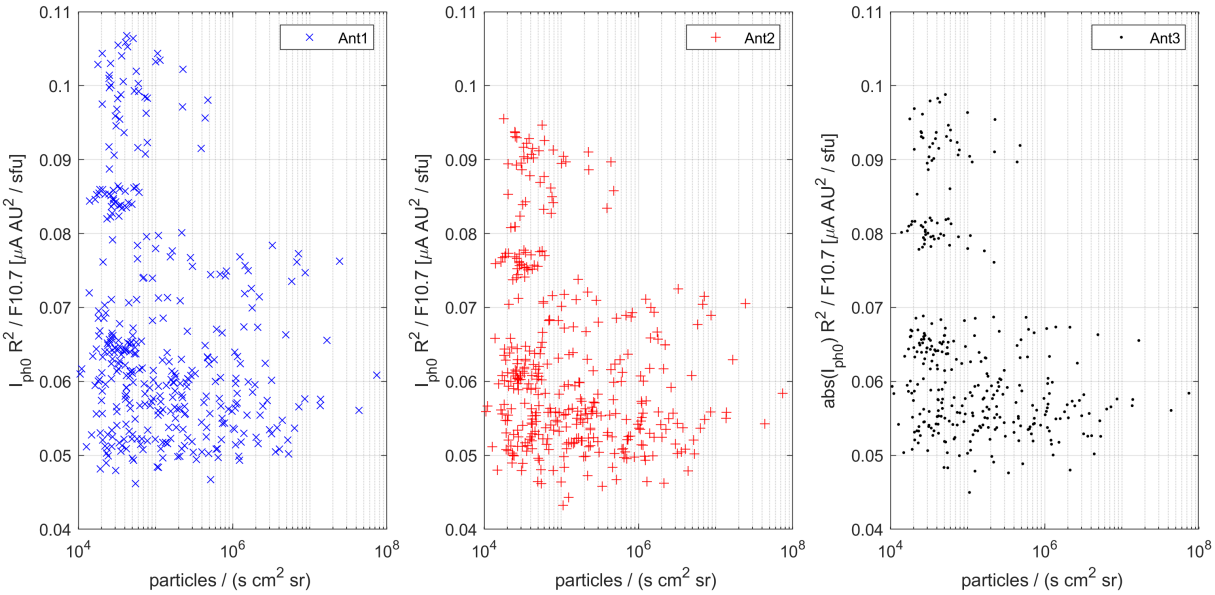

Figure 14: Datapoints of the normalized I_{ph0} plotted against the respective energetic particle flux at that time for all three antennas.

4.5 Influence of material properties

As mentioned in section 3.5, apart from solar illumination, desorption and material decomposition are expected to have an effect on I_{ph0}. As desorption has a much lower activation energy (4-40 kJ/mol) than decomposition (80-320 kJ/mol) [11], we expect to see the combined effect of two processes, one fast and one slow. However, material parameters such as the exact energies required and whether they are affected by temperature is difficult to predict, and thus we approach this problem by testing a time dependent model against the available data. Specifically, we aim to find the time dependencies t_d of the two expected processes so as to be able to predict how material degradation due to outgassing will impact future performance of the antennas of SolO's RPW instrument.

As such processes may not only depend on time but on temperature as well, we also tried to build a model that takes changes in temperature with SolO's distance to the Sun into account. This was done as a bonus part of the project, and did not yield any usable results or predictions about the future behaviour of I_{ph0}. However, it illustrates how such a model could theoretically be created and which difficulties arise in practice when using an actual data set as input.

4.5.1 Time dependent model

For a model where changes in material properties due to outgassing are solely dependent on time, we disregard any potential dependence on temperature, and try to fit a curve of the form

$$I_{\text{ph0}} = ae^{-t/t_{d,1}} + be^{-t/t_{d,2}} \tag{5}$$

to the data, where a and b are constants, t is the time and $t_{d,i}$ are the time dependencies of the two respective processes. For this we use the fit() function in Matlab with an "exp2"

fittype, which assumes the data to follow a two-term exponential form such as the one shown above. As can be seen in fig. 15, this was only possible for the data from June 2020 onwards, whereas a dependence on the distance R to the Sun, which in turn was time dependent during this period, could be found for the datapoints before that. Fig. 16 shows how the time dependent model quickly diverges from these earlier datapoints. However, the main relevance lies in the model for the later period and what can be extrapolated from it in terms of future behaviour of I_{ph0}. From June 2020 onwards, although the precise constants differ for the antennas, all three antennas seem to follow this two-term exponential behaviour in a purely time dependent fashion. This model indicates a time dependence of about three weeks, with variation between 14.9 to 24.4 days depending on the antenna, for the fast process, which we assume to be desorption of water and other outgassing products from the antenna surfaces. The slower process, which we assume to be decomposition of the antenna material itself, has a time dependence of 976.2 to 1466.4 days, or between two and a half to four years.

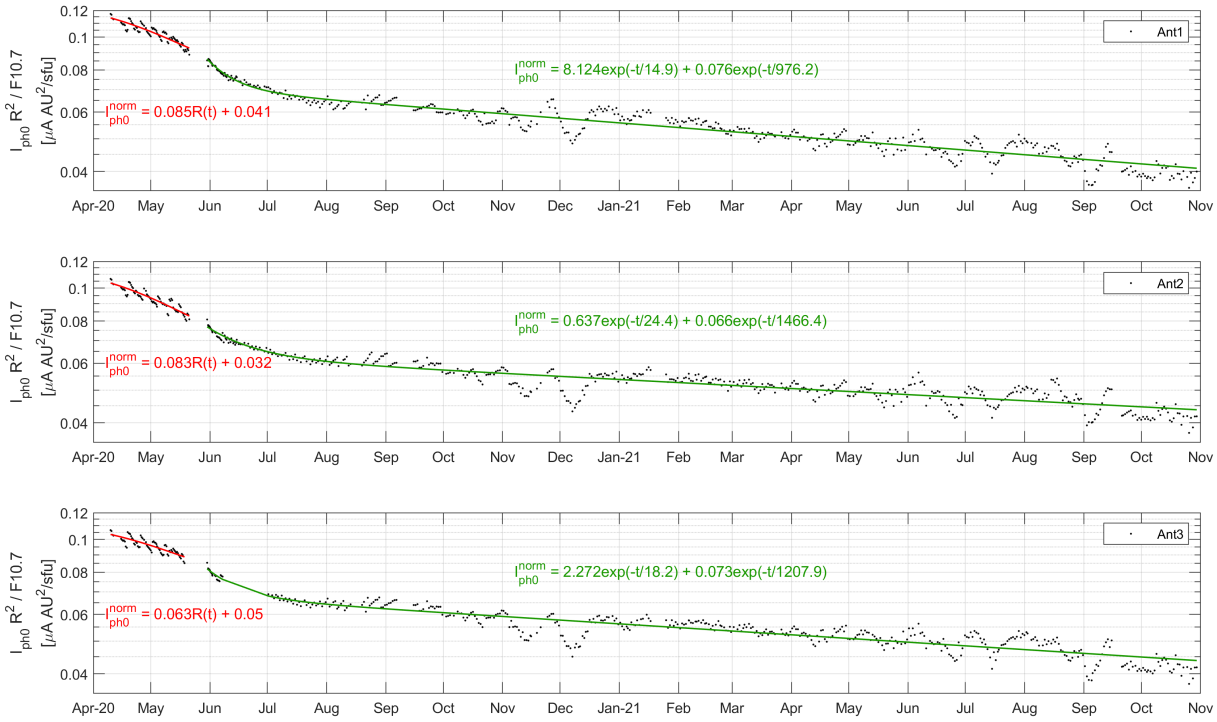

Figure 15: I_{ph0} data (black dots) with a two-term exponential model (green line) fitted from June 2020 onward, along with a $R(t)$-dependent exponential model (red line) for the earlier period. Note that the fit functions differ somewhat between the three antennas.

Continuing along this trend leads to the prediction shown in fig. 16, which shows a time frame from the start of the mission until one year into the extended mission phase. By then, according to this model, I_{ph0} will have reached levels about a fifth of the levels it had at the end of 2021.

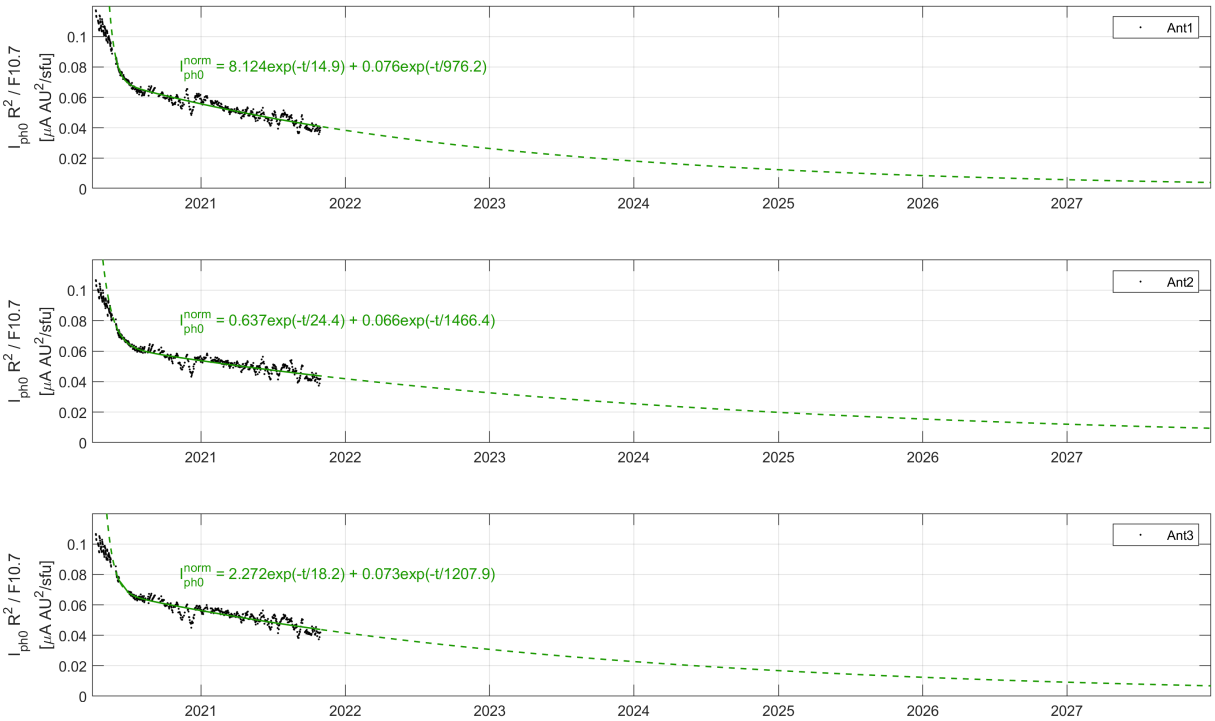

Figure 16: I_{ph0} data (black dots) and prediction of the future behaviour of I_{ph0} assuming a purely time dependent model (green dashed line).

4.5.2 Temperature dependent model

For the temperature dependent model, we first acknowledge that the change of I_{ph0} with time will depend on both the initial amplitude of I_{ph0} and some function of temperature $f(T)$ of yet unknown form, and thus follow the relation

$$\frac{\mathrm{d}I_{\mathrm{ph0}}}{\mathrm{dt}} = I_{\mathrm{ph0}} f(T) \tag{6}$$

This can be rewritten as

$$f(T) = \frac{1}{I_{\mathrm{ph0}}} \frac{\mathrm{d}I_{\mathrm{ph0}}}{\mathrm{dt}} = \frac{\mathrm{d}}{\mathrm{dt}} \ln(I_{\mathrm{ph0}}) \tag{7}$$

We also know from the Stefan-Boltzmann law that intensity of radiation is proportional to T^4, and, through the inverse square law, inversely proportional to R^2. From this, we can summarize the correlation between distance and temperature as $T^4 \propto \frac{1}{R^2}$ or, in simpler terms, $T \propto \frac{1}{\sqrt{R}}$. From this, we have

$$f(T) = g\left(\frac{1}{\sqrt{R(t)}}\right) \tag{8}$$

where g is a new function that is different from f and depends on the distance R from SolO to the Sun, which, in turn, is time dependent.

In order to find an expression for I_{ph0} that includes a temperature dependence but can be expressed indirectly through the time dependent variable R, we now integrate eq. 7 and then take the exponential of it while inserting the relation from eq. 8, getting first

$$\ln(I_{\text{ph0}}) = \int_0^t \frac{\mathrm{d}}{\mathrm{dt}} \ln(I_{\text{ph0}})\, dt = \int_0^t f(T)\, dt \tag{9}$$

and then

$$I_{\text{ph0}} = \exp(\ln(I_{\text{ph0}})) = \exp\left(\int_0^t f(T)\, dt\right) = \exp\left(\int_0^t g\left(\frac{1}{\sqrt{R(t)}}\right) dt\right) \tag{10}$$

While this is mathematically easy to do, when building a model based on preexisting data, it must be done numerically, which introduces difficulty as any error will propagate and increase with each step. In Matlab, we approach this by first limiting our data to after June 15th 2020, as earlier data includes large variations and, furthermore, when it comes to predicting the future behaviour of I_{ph0} we are more interested in contributions from more recent behaviour. This leaves us with 458 datapoints for antennas one and two respectively, and 441 for antenna three. We therefore illustrate this method using only data from antenna one.

At this point we had to smooth our data considerably with Matlab's smooth() function using a span of 23, meaning that the smoothing occurs based on 23 neighbouring datapoints. While this introduces more uncertainty into the results, it is what enables the subsequent steps in Matlab. We now take the logarithm and then derivative of the smoothed data to get $\frac{\mathrm{d}}{\mathrm{dt}}\ln(I_{\text{ph0,d}})$, where we introduce the subscript "d" for the data, and henceforth use subscript "m" for the model.

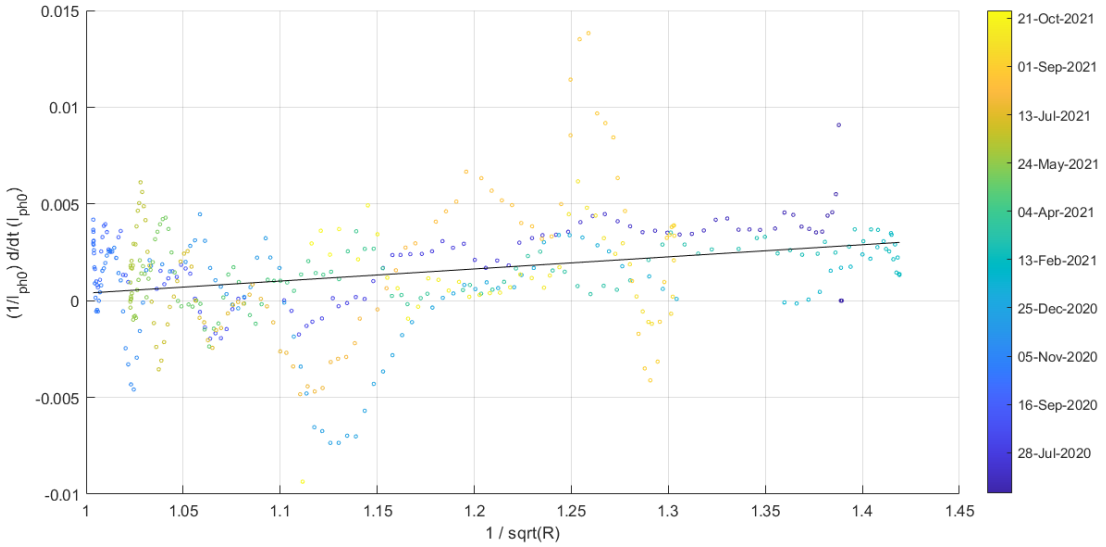

Figure 17: Datapoints with their chronological order indicated by the colour bar, and the model function g_m as a linear fit.

As indicated in eq.7 and eq. 8, we have, for our data, the situation that

$$\frac{\mathrm{d}}{\mathrm{dt}}\ln(I_{\text{ph0,d}}) = \frac{1}{I_{\text{ph0,d}}}\frac{\mathrm{d}I_{\text{ph0,d}}}{\mathrm{dt}} = f_d(T) = g_d\left(\frac{1}{\sqrt{R_d(t)}}\right) \tag{11}$$

where the two expressions on the left are time dependent, while f is temperature dependent, and g is a distance dependent function different from f. In order to go from our data to a model, we plot $\frac{\mathrm{d}}{\mathrm{dt}}\ln(I_{\mathrm{ph0,d}})$ against $1/\sqrt{R}$ to find g_d, and fit a straight line to the data as shown in fig. 17 to establish our model g_m.

Inserting this g_m and the values $R_m(t)$ obtained from it into eq. 10 and performing the necessary mathematical operations, we can now theoretically get $I_{\mathrm{ph0,m}}$, meaning that we go from

$$\frac{\mathrm{d}}{\mathrm{dt}}\ln(I_{ph0,m}) = g_m\left(\frac{1}{\sqrt{R_m(t)}}\right) \tag{12}$$

to

$$I_{\mathrm{ph0,m}} = \exp\left(\int_0^t g_m\left(\frac{1}{\sqrt{R_m(t)}}\right)\,dt\right) \tag{13}$$

However, while a seemingly linear trend can be clearly made out in the data in the above figure, and g_m can be easily established as a linear fit, when doing the further mathematical operations, the result is incredibly sensitive to the exact slope and height of g_m. Using g_m to define values $1/\sqrt{R_m(t)}$ and then reordering them chronologically, we integrate $g_m(1/\sqrt{R_m(t)})$ in Matlab by multiplying its value at the time t with the time until the next datapoint, and then sum those values. Next, we take the exponential of the result. However, the model defined by the above g_m does not yield any result in good or even just acceptable correlation with the data. Even when changing g_m tremendously, no sensible result can be obtained with this method.

5 Discussion

In the previous section, we have normalized the I_{ph0} time series with respect to various parameters that might influence it, and then tried to find an explanation for the remaining variation. In this section, we discuss these results further.

5.1 Variation with solar illumination

After normalizing for variations in distance of SolO to the Sun, we also normalized with respect to variations in solar activity, based on measurements of the $\mathrm{F}_{10.7}$ index from Earth. The results in section 4.2 show that a weighted timeshift of the $\mathrm{F}_{10.7}$ index values, including both a forwards- and backwards shift to allow a point on the solar equator to rotate from facing Earth to SolO or the other way around, weighted by how long the respective other timeshift is, results in the smoothest I_{ph0} time series. This was thus assumed to be the best normalization and most accurate representation of how I_{ph0} in the three antennas changes with time when variations due to solar illumination are omitted.

From these timeshifted datapoints, a dependence of I_{ph0} on solar activity could be extracted. We show that the amplitude of I_{ph0} depends roughly linearly on solar activity, but that the exact proportionality changes with time. This rather pronounced change is already noticeable from less than two years of data. The change is two-fold: both the

overall amplitude of I_{ph0} for a specific level of solar activity as well as the slope of the proportionality decrease with time. In summary, all three antennas of the ANT subsystem of RPW react progressively less strongly to solar activity with time, and we can conclude that there must be some effect yet unaccounted for that facilitates this.

While the timeshift of the $\mathrm{F}_{10.7}$ index values proves useful in normalizing the I_{ph0} time series and make further statements about long-term behaviour of I_{ph0}, it also introduces a lot of uncertainty into further investigations, especially those of phenomena that occur on much shorter timescales than a solar rotation, such as solar flares and variations in energetic particle flux.

5.2 Influence of solar flares

In section 4.3, we could not find any indication that solar flares had a discernable effect on I_{ph0}. Neither did the flares reliably coincide with peaks in the I_{ph0} data, nor did we see higher peaks for higher X-ray class solar flares. However, this also does not completely preclude the possibility of such a connection, as many uncertainties are present in this work that may obscure such an effect:

First, it is possible that the observed flares were simply not intense enough to be notable, but that higher X-ray class flares would have a noticeable effect. Also, X-ray class does not reliably scale with intensity across the entire wavelength spectrum that may influence I_{ph0}, and different wavelength are differently dimmed by limb darkening in the case of an AR location on the limb. Furthermore, different wavelengths may peak at different times before, during or after a flare. For example, EUV usually occurs a few minutes after the maximum X-ray output, but also, the entire active region exhibits variation in output around the flare event itself. It is possible that some of the flares in our data set, in particular the ones on August 28th and October 9th 2021, may indirectly show themselves in the I_{ph0} time series, as those flares were of roughly equal X-ray class and both peaked around six hours before the I_{ph0} datapoint from their respective day was measured.

Furthermore, our sample of 22 solar flares was quite low, and as such events take only minutes to an hour while I_{ph0} is measured only once a day it is possible that any effect of solar flares on I_{ph0} could simply have been missed entirely.

Finally, the approximative nature of the normalization by a timeshifted $\mathrm{F}_{10.7}$ index must be kept in mind. Although the weighted timeshift was the best available option, solar activity in a specific region may change considerably while it faces away from Earth, meaning that even peaks in the I_{ph0} time series that seemingly happen to coincide with a solar flare need not truly have that exact shape and position. However, as solar flares tend to occur over active regions, which also show themselves as a heightened $\mathrm{F}_{10.7}$ index, we can still expected them to show up in the data in close proximity to each other, as they are causally connected. Nonetheless, as even for the I_{ph0} values only normalized with respect to distance R to the Sun, and not the timeshifted $\mathrm{F}_{10.7}$ values, no significant features coincide with a solar flare, this shows that any effect of flares on I_{ph0} is, if present, far weaker than that of overall solar activity.

We conclude that the observed solar flares, insofar as they were registered by RPW, are unlikely to have a strong effect on I_{ph0}, as any variation is within the level of the background noise. More conclusions about any possible connection could be drawn if we

had a larger sample of flares. This is likely to increase over the coming years as we head towards solar maximum. With more flares, and especially flares from the time of day when I_{ph0} is measured and from time periods where the angle between SolO and Earth is small, would make the dataset more conclusive.

5.3 Influence of energetic particle impacts

As energetic particle fluxes in section 4.4 varied on rather short temporal scales for both electrons and ions, both separately as well as combined, correlations with I_{ph0} could not be identified. In particular, some notable increases in electron flux did not line up with increases in I_{ph0}, but rather with decreases, which is counterintuitive as particles are thought to transfer energy to the probe. One explanation for this might be that the weighted timeshift of $\mathrm{F}_{10.7}$ is simply wrong for the particular time of those features, so that what looks like a valley should actually be a peak. This is a possibility as solar activity could have changed on short timescales while the active region was facing away from Earth and towards SolO. Another explanation would be that electron fluxes simply do not affect I_{ph0} in any way that is discernable from this data, and that any effect is of purely radiative origin.

As no correlation with ion or combined fluxes could be discerned either, we conclude that particle fluxes do not significantly impact I_{ph0} at a level that would be distinguishable from stronger influences by other parameters. In particular, when plotting particle fluxes directly against I_{ph0}, variations between individual antennas as well as the previously noted trend of earlier I_{ph0} measurements being systematically higher both exceed any dependence I_{ph0} may have on energetic particle fluxes. One way to investigate a possible correlation between I_{ph0} and energetic particle impacts further might be to normalize I_{ph0} with respect to the model found in section 4.5.1, and see if any new patterns emerge.

5.4 Influence of material properties

In section 4.5.1 we fit a two-term exponential function to the normalized I_{ph0} time series in order to model the remaining I_{ph0} variation as two co-occurring processes of material degradation. We find a fast process, which we assume to be desorption of water and other outgassing products from the antenna surfaces, with a time dependence of about three weeks, and a slower process, which we assume to be decomposition of the antenna material itself, with a time dependence between two and a half to four years depending on the antenna. These two time scales of a few weeks and a few years respectively are both in line with expectations for outgassing of materials on spacecraft [11]. Such a time dependent fit being found implies that there is no strong temperature dependence of the two processes within the temperature range experienced by SolO so far.

This model predicts I_{ph0} to reach levels about a fifth of its current ones within the next six years. Such a large decrease of I_{ph0} could have a high impact on the quality of future measurements with RPW, as the bias current fed to the probe will have to be adjusted ever more precisely to remain below the decreasing I_{ph0}. As solar maximum will occur towards the end of the nominal mission phase, solar activity will be comparably higher. Therefore, we can expect I_{ph0} to be comparably higher as well, which might mitigate the effects of material degradation to some degree. However, closer to a full solar cycle of

11 years after the start of the mission, we face another solar minimum, meaning that towards the end of the extended mission phase and the phase following after, if SolO is still operational, the effects will become increasingly noticeable.

As a bonus part of the project, in section 4.5.2 we tried to find a temperature dependent model as well. While mathematically possible, this proved difficult in practice, and did not yield any usable results even when manually adjusting the parameters of the model. It is also difficult to improve the strategy for building this model, as the method is so sensitive to even small initial errors or variations in the input data. Several steps in the calculations cause errors to not only propagate but also increase, sometimes exponentially. More datapoints and a more sophisticated mathematical approach, especially for the steps where we integrate and take the exponential of a currently already error-ridden result, might mitigate this to some degree, and make it possible to find a T-dependent model for I_{ph0}. However, as the two models stand currently, the purely time dependent one is in better agreement with the data, and therefore the better option for making predictions as to the future behaviour of I_{ph0}.

6 Conclusion

In this project, we have investigated the dependence of I_{ph0} on solar illumination as well as solar flares and energetic particle impacts, and then modeled the remaining I_{ph0} variation in order to make predictions of its future behaviour. Predicting I_{ph0} is important for operating the RPW instrument in an optimal fashion and thus ensure good measurements of for example electric fields. Long-term predictions can also be indicative of how long the instrument will remain operational.

To account for the effects of solar illumination, we normalized the I_{ph0} data with respect to both SolO's distance to the Sun, and solar activity as indicated by the $\text{F}_{10.7}$ index. As the Sun may have active regions that, if Earth and SolO are at different angles from the Sun, face them at different times, we extrapolated how $\text{F}_{10.7}$ would have varied at SolO based on the measurements from Earth. For this we first compensated for difference in distance to the Sun and then used a weighted timeshift that moved each datapoint both forwards and backwards in time, weighted with how long the respective other shift was, in order to both simulate the Sun rotating so the side observed from Earth instead faces SolO, and also account for the increased likelihood of the activity changing if the solar equator has to rotate longer before or after the region faced SolO. While the resulting normalized I_{ph0} time series was not completely smooth, it was a better option than a simple forwards- and backwards shift of the $\text{F}_{10.7}$ datapoints in an attempt to align notable features in I_{ph0} with peaks and valleys in the $\text{F}_{10.7}$ measurements from Earth, or than simply shifting each datapoint the shortest possible time to align it with SolO. The time series from the weighted timeshift shows that even when I_{ph0} is normalized with respect to variation due to solar illumination, it still keeps decreasing with time due to some other effect.

In this work, no correlation between solar flares and I_{ph0} could be established from the available data. However, we note that this also does not preclude such an effect, as our sample size of 22 flares was very small, and flares may have occurred at other times of day than when the I_{ph0} datapoint was taken. Furthermore, uncertainty introduced by the weighted timeshift may obscure a possible correlation. No discernable effect of energetic

particle impacts on I_{ph0} could be found either, and it was furthermore shown that such an effect, if present, would be far weaker than the measured effects caused by variations in other parameters.

We modeled the remaining I_{ph0} variation as two co-occurring processes of material degradation, where desorption of water and other outgassing products from the antenna surfaces occurs with a time dependence of about three weeks, with variation between 14.9 to 24.4 days depending on the antenna, and decomposition of the antenna material itself has a time dependence of 976.2 to 1466.4 days, or between two and a half to four years. While temperature can sometimes be a driving factor for such degradation processes, finding a time dependent fit that agrees with the data suggests that no strong temperature dependence exists for the two processes within the temperature range experienced by SolO so far. The model predicts a significant lowering of I_{ph0} to about one fifth of its current values before the end of the nominal mission phase in a little more than five years time. Such a significant decrease in I_{ph0} will make operating the RPW instrument more difficult. As the later part of the nominal mission phase coincides with solar maximum however, when solar illumination and thus I_{ph0} can be expected to be higher, these effects may not become problematic until the extended mission phase, when we approach solar minimum again. As time progresses, with more datapoints of I_{ph0} and the corresponding solar activity, this model could be adjusted and made more accurate, and more reliable predictions obtained.

Acknowledgements

Most of all, I want to thank my supervisor, Niklas Edberg, for being so attentive and helpful throughout the entire project, from introducing me to MatLab and helping me get the code to run to discussing the results and giving me feedback on the report. I learned a lot during this project and that is only possible when someone really invests time in you and your learning process.

I also want to thank Anders Eriksson for giving the guest lecture that made me want to seek out a project at IRFU, and for being so enthusiastic and full of ideas when encouraging me to try my hand at the temperature dependent model.

Furthermore I thank Andreas Korn, my examiner, for encouraging us students to do project courses like this from day one.

Finally, I thank Robert C. Allen from the Johns Hopkins University and Robert Wimmer-Schweingruber from Kiel University for providing me with the EPD data.

This work was (partly) carried out by using Hinode Flare Catalogue (https://hinode.isee.nagoya-u.ac.jp/flare_catalogue/), which is maintained by ISAS/JAXA and Institute for Space-Earth Environmental Research (ISEE), Nagoya University.

References

[1] Müller, D. et al. "The Solar Orbiter mission - Science overview". In: *A&A* 642 (2020), A1. DOI: 10.1051/0004-6361/202038467.

[2] Garcıa Marirrodriga, C. et al. "Solar Orbiter: Mission and spacecraft design". In: *A&A* 646 (2021), A121. DOI: 10.1051/0004-6361/202038519.

[3] Yu. V. Khotyaintsev et al. "Density fluctuations associated with turbulence and waves. First observations by Solar Orbiter". In: *A&A* (2021). Forthcoming article. DOI: 10.1051/0004-6361/202140936.

[4] Maksimovic, M. et al. "The Solar Orbiter Radio and Plasma Waves (RPW) instrument". In: *A&A* 642 (2020), A12. DOI: 10.1051/0004-6361/201936214.

[5] K. F. Tapping. "The 10.7 cm solar radio flux (F10.7)". In: *Space Weather* 11.7 (2013), pp. 394–406. DOI: 10.1002/swe.20064.

[6] Thiemann, E. M. B. et al. "Center-to-Limb Variability of Hot Coronal EUV Emissions During Solar Flares". In: *Solar Physics* 293.19 (Jan. 2018). DOI: 10.1007/s11207-018-1244-2.

[7] Edberg, N. J. T. et al. "Solar flares observed by Rosetta at comet 67P/Churyumov-Gerasimenko". In: *A&A* 630 (2019), A49. DOI: 10.1051/0004-6361/201834834.

[8] W. T. Thompson. "Coordinate systems for solar image data". In: *A&A* 449.2 (Apr. 2006), pp. 791–803. DOI: 10.1051/0004-6361:20054262.

[9] SpaceWeatherLive - Parsec vzw. *Top 50 solar flares of the year 2021.* (Accessed: 2021-06-14 and 2021-11-01). URL: https://www.spaceweatherlive.com/en/solar-activity/top-50-solar-flares/year/2021.html.

[10] Rodrıguez-Pacheco, J. et al. "The Energetic Particle Detector - Energetic particle instrument suite for the Solar Orbiter mission". In: *A&A* 642 (2020), A7. DOI: 10.1051/0004-6361/201935287.

[11] Schläppi, B. et al. "Influence of spacecraft outgassing on the exploration of tenuous atmospheres with in situ mass spectrometry". In: *Journal of Geophysical Research: Space Physics* 115.A12 (2010). DOI: 10.1029/2010JA015734.

[12] N. Papitashvili. *Interface to produce plots, listings or output files from OMNI 2.* (Accessed: 2021-06-08 and 2021-11-01). URL: https://omniweb.gsfc.nasa.gov/form/dx1.html.

[13] S. Masuda et al. *Hinode Flare Catalogue.* (Accessed: 2021-06-14). URL: https://hinode.isee.nagoya-u.ac.jp/flare_catalogue/.